Optical bistability and flip-flop function in feedback Fano laser

Liang, Shih Lun; Mørk, Jesper; Yu, Yi

Published in:
Optics Express

Link to article, DOI:
10.1364/OE.510599

Publication date:
2024

Document Version
Publisher's PDF, also known as Version of record

Research Article | Vol. 32, No. 5 / 26 Feb 2024 / Optics Express 8230
Optics EXPRESS

Optical bistability and flip-flop function in feedback Fano laser

SHIH LUN LIANG,[1,2] JESPER MØRK,[1,2,3] AND YI YU[1,2,4]

[1]DTU Electro, Technical University of Denmark, Lyngby, Denmark
[2]NanoPhoton – Center for Nanophotonics, Technical University of Denmark, Lyngby, Denmark
[3]jesm@dtu.dk
[4]yiyu@dtu.dk

Abstract: Optical bistability has the potential to emulate the capabilities of electrical flip-flops, offering plenty of applications in optical signal processing. Conventional optical bistable devices operate by altering the susceptibility of a nonlinear medium. This method, however, often results in drawbacks such as large device size, high energy consumption, or long switching times. This work proposes an optical bistable device incorporating strong optical feedback into a Fano laser. This leads to multiple stable states and introduces a region of bistability between the inherent Fano mode and a feedback-induced Fabry-Perot mode. Unlike conventional bistable devices, the Fano system exploits strong field localization in a nanocavity to control the properties of one of the laser mirrors. This configuration means that switching states can be achieved by modulating the mirror's loss rather than changing the susceptibility of the active medium. Importantly, modulation can be implemented locally on a nanocavity, bypassing the need to adjust the entire laser system. This leads to fast flip-flop actions with low energy consumption. The feedback Fano laser can be embodied in a compact microscopic structure, thus providing a promising approach towards integrated all-optical computation and on-chip signal processing.

1. Introduction

Bistability refers to devices or systems that possess two stable equilibrium states, with the actual operating state determined by the initial condition. This property is foundational in digital electronics, facilitating binary data storage and serving as a cornerstone for random-access memory and computers [1]. An optical counterpart would be significant for switching, routing, memory, pulse shaping, and logic operations [2]. These tasks underpin all-optical computing architectures aiming to eliminate power-draining electrical-to-optical conversions [3]. Previous optical bistable devices such as semiconductor optical amplifier (SOA)-MZI [4,5], coupled ring laser [6], and photonic crystal microcavity structure [7] exploited either the change of the real (refractive index) [7–9] or imaginary (gain/absorption) [5,10,11] part of the susceptibility of a nonlinear medium. Typically, these designs feature large footprints, high energy consumption, or long switching times in order to achieve a sufficiently large change in the mode-averaged susceptibility.

Here, we propose a bistable device that enables state switching based on altering the 'laser's mirror loss. This is achieved through an optical Fano resonance [12,13] generated by coupling a nanocavity (NC) with a waveguide (WG). The original Fano laser [14,15] has shown plenty of phenomena, such as self-pulsation [16], narrow linewidth [17], and improved stability towards unintended optical feedback [18]. Also, the same Fano resonance can be used to implement several all-optical signal processing functionalities [19]. Compared to the original Fano laser configuration, where the WG is closed on one side and open on the other, in the feedback Fano laser considered here (Fig. 1(a)), the WG is closed on the left side and partially blocked on the right side. This leads to strong external feedback into the original Fano laser mode. Our current study contrasts with the weak feedback system we investigated earlier [18]. This configuration

#510599 https://doi.org/10.1364/OE.510599
Journal © 2024 Received 9 Nov 2023; revised 17 Jan 2024; accepted 7 Feb 2024; published 22 Feb 2024

Optics EXPRESS

introduces multiple modes in addition to the original Fano mode, resulting in bistability between Fano and Fabry-Perot (FP) modes. By harnessing the unique properties of the Fano mirror, we show that by modulating the NC resonance, one can effectively control the laser bistability, leading to fast flip-flop operations with minimized energy consumption.

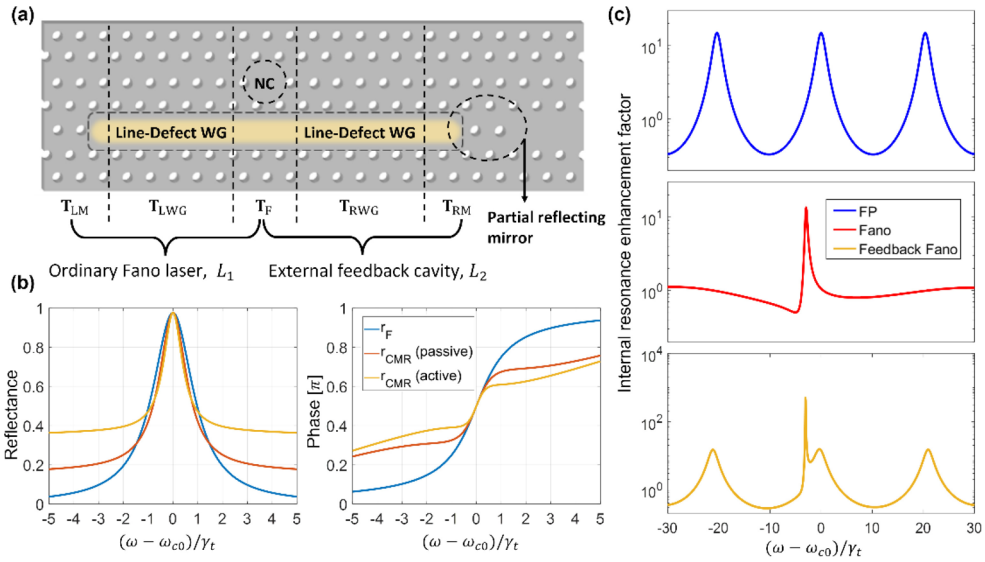

Fig. 1. (a) Schematic of the feedback Fano laser realized in a 2-D photonic crystal slab. A nanocavity (NC) of H1 type (one missing air hole) is side-coupled to a closed line-defect waveguide (WG). The WG has an almost completely reflecting mirror at the left end and a partially reflecting mirror at the right end. The entire device functions as a conventional Fano laser with a length of L_1, complemented by an external feedback cavity of length L_2. The light yellow area represents the active region. (b) Fano mirror and composite Fano mirror reflectance and phase change as a function of normalized frequency detuning $(\omega - \omega_{c0})/\gamma_t$, where γ_t is the linewidth of the nanocavity mode and ω_{c0} is the original NC resonance frequency without shifting. The blue lines represent the ordinary Fano mirror without feedback. The red lines represent the passive composite Fano mirror. The yellow lines represent the active composite Fano mirror when carrier density $N = 5N_0$, where N_0 is the transparency carrier density.(c) Comparison of the internal resonance enhancement factor, A_r, for the Fabry-Perot (FP) cavity (blue), Fano laser cavity (red), and feedback Fano cavity (yellow) in dependence of the frequency detuning.

2. Feedback Fano laser system

2.1. Design and the oscillation modes

Figure 1(a) illustrates the structure of the feedback Fano laser. A passive NC is side-coupled to a WG, which can be realized in different platforms, such as two-dimensional photonic crystal membranes [20] or one-dimensional nanobeam structures [21–23]. The left-hand-side (LHS) and right-hand-side (RHS) reflections can be implemented by, e.g., the photonic band gap effect, which leads to broadband mirrors. The active material, such as quantum dots or quantum wells, is embedded only within the WG, which can be implemented by buried heterostructure nanotechnology [24–27]. Choosing the WG length such that the field from the NC (a discrete mode) and the field propagating in the WG (a continuum of modes) interfere destructively, the oscillation condition can be met at the NC resonance frequency [14,19]. Therefore, a highly

Optics EXPRESS

reflective "mirror" with a narrow bandwidth determined by the decay rate of the NC mode is formed, which we refer to as the Fano mirror.

In contrast to an ordinary Fano laser [15,19], whose WG is open on the right end, our device has a second reflection surface at the far right, with a lower reflectivity than the left one. Such a closed WG configuration generates a background of FP longitudinal modes superimposed with the narrowband Fano resonance originating from the side-coupled nanocavity. As a result, multiple modes with close oscillation frequencies can emerge, as illustrated by the internal resonance enhancement factor [28], defined as the ratio of the field intensity transmitted into the cavity to the intensity of the field circulating within the cavity. This can be expressed as $A_r = 1/|1 - r_1 r_2 \exp(-2ikL)|^2$(valid for any two-mirror cavity with reflection coefficients r_1, r_2, and length L) (Fig. 1(c)). In the feedback Fano cavity, the Fano mode and FP mode thus coexist. These modes compete in a laser, and the dominant mode is determined by the one with the lowest threshold gain.

We want to highlight that the feedback Fano laser system presented here differs fundamentally from a dual-coupled cavity system [29]. The latter operates on weak coupling, wherein the interaction between cavities does not significantly modify the original cavity mode field. On the other hand, our system exhibits a pronounced coupling between the NC and the WG. For instance, the NC induces a π phase shift in the WG field (the NC "cuts" the WG into two), which effectively transforms an initial anti-mode of the WG into a resonance mode, as detailed in [30]. When correlating with the traditional q parameter characteristic of the Fano resonance [13], our q parameter is effectively zero [19,30]. This is because our configuration lacks any partial reflection element within the waveguide. Furthermore, we've assumed identical nanocavity-waveguide coupling rates for both the RHS and LHS. Compared to the weak feedback system [18], the structure investigated here has strong and intentional optical feedback, meaning that multiple reflections in the external cavity formed between the Fano mirror and the right reflection must be considered. The eigenmodes of the laser can be identified using the transmission matrix (T-matrix) approach [31]. The overall T-matrix of the feedback Fano laser (Fig. 1(a)) is the product of the individual elements, $\mathbf{T} = \mathbf{T}_{LM}\mathbf{T}_{LWG}\mathbf{T}_F\mathbf{T}_{RWG}\mathbf{T}_{RM}$, with

$$\begin{aligned}
&\mathbf{T}_{LM}=\tfrac{1}{t_L}\begin{pmatrix} 1 & -r_L \\ -r_L & 1 \end{pmatrix}, \quad \mathbf{T}_{LWG}=\begin{pmatrix} \exp[-ik(\omega,N)L_1] & 0 \\ 0 & \exp[ik(\omega,N)L_1] \end{pmatrix}, \\
&\mathbf{T}_{RWG}=\begin{pmatrix} \exp[-ik(\omega,N)L_2] & 0 \\ 0 & \exp[ik(\omega,N)L_2] \end{pmatrix}, \quad \mathbf{T}_{RM}=\tfrac{1}{t_R}\begin{pmatrix} 1 & r_R \\ r_R & 1 \end{pmatrix}, \\
&\mathbf{T}_F=\tfrac{1}{t_F(\omega)}\begin{pmatrix} 1 & -r_F(\omega) \\ r_F(\omega) & t_F^2(\omega)-\mathrm{r}_F^2(\omega) \end{pmatrix}.
\end{aligned} \tag{1}$$

Here, the subscript LM and RM represent the LHS and RHS mirror, LWG and RWG represent the LHS and RHS WG, and F represents the Fano mirror, respectively. $r_L(t_L)$ and $r_R(t_R)$ are the reflection (transmission) coefficients of the WG's left and right end mirrors. L_1 and L_2 are the lengths of the LHS and RHS of the WG. ω is the field oscillation frequency. The Fano mirror's reflection and transmission coefficients found using temporal coupled-mode theory [15,32] are

$$r_F(\omega) = \frac{i\gamma_c}{i\delta(\omega)+\gamma_t}, \qquad t_F(\omega) = \frac{\delta(\omega)-i\gamma_v}{i\delta(\omega)+\gamma_t}, \tag{2}$$

where $\delta(\omega) = \omega_c - \omega$ is the detuning between the field and the NC resonance frequency ω_c. $\gamma_c = \omega_{c0}/(2Q_c)$ and $\gamma_v = \omega_{c0}/(2Q_v)$ denotes the decay rates of the NC due to WG coupling and its intrinsic loss, with corresponding Q-factors of Q_c and Q_v, respectively. The total NC decay rate is $\gamma_t = \gamma_c + \gamma_v$. Here, ω_{c0} is the NC frequency, identical to the lasing frequency of an

Optics EXPRESS

ordinary Fano laser without feedback, where its threshold gain is at a minimum (perfect phase matching) [14]. We take it as the reference for the NC frequency detuning. Note that the transfer matrices, $\mathbf{T}_{LWG}$ and $\mathbf{T}_{RWG}$, are functions of the complex wave number $k(\omega, N)$ of the WG mode and thus depend on the carrier density, N,

$$k(\omega, N) = \frac{n}{c}\omega - \frac{i}{2}[(1 - i\alpha)\Gamma g_n(N - N_0) - \alpha_i]. \tag{3}$$

Here, n is the refractive index, c is the speed of light, α is the linewidth enhancement factor due to amplitude-phase coupling [33], Γ is the optical confinement factor, g_n is the differential gain coefficient under linear approximation, N_0 is the transparency carrier density, and α_i is the internal propagation loss. We simplify our analysis by assuming the laser operates in the region where the dispersion of the waveguide is not affected by slow-light effects, which may be important in (active) photonic crystal waveguides, depending on the operating wavelength [34]. Such effects can be minimized using a nanobeam geometry, as detailed in [23]. Based on Eqs. (1)-(3), one can obtain an analytical formulation of the device's transmission spectrum. Specifically, the overall T-matrix is first transformed into the scattering S-matrix, whose poles determine the eigenmodes. Such poles correspond to lasing for an active device [31]. The overall S-matrix has a shared denominator T_{11}, making it simple to determine the poles. As a result, the oscillation condition of a feedback Fano laser can be rewritten as (see Supplement 1, section 1)

$$\begin{aligned} &\exp[2ik(\omega, N)L_1]r_L r_F(\omega) + \exp[2ik(\omega, N)L_2]r_R r_F(\omega) \\ &+ \exp[2ik(\omega, N)(L_1 + L_2)]r_L r_R[t_F^2(\omega) - r_F^2(\omega)] = 1 \end{aligned}. \tag{4}$$

The first (second) term in Eq. (4) can be recognized as the propagation factor when the field propagating in the LHS (RHS) WG encounters the LHS (RHS) mirror and the Fano mirror, and the third term represents the coupling between the field dwelling in the entire WG and the NC. From Eq. (4), we can calculate the oscillation frequency of all the modes of the system and their corresponding threshold carrier densities.

We consider two cases of low ($r_R = 0.3$) and high ($r_R = 0.7$) RHS mirror reflectivity. Figure 2 shows all the calculated modes when tuning the (normalized) NC frequency detuning $\sigma_c = (\omega_c - \omega_{c0})/\gamma_t$ (all simulation parameters are provided in Table S1 in Supplement 1 unless otherwise specified). The horizontal dotted lines in Figs. 2(a) and 2(c) represent the longitudinal modes of the left and right mirrors when the NC is transparent. These are FP modes with a free spectral range that equals $20.5\gamma_t$ for the specific choice of parameters.

According to the presence and threshold gains of the lasing modes, Figs. 2(a) and (b) can be divided into three regions: Fano mode region (the exclusive lasing mode is the Fano mode, as discussed later), bistability region (either the Fano or the FP mode can lase), and FP mode region (the lasing mode is the FP mode). The boundaries between these regions correspond to the points at which either the green curve (LHS-Fano mode) or the violet curve (FP mode) end (Fig. 2). In the Fano mode region, the NC frequency ω_c is close to ω_{c0}, and there are two (Fano) modes whose oscillation frequencies depend almost linearly on ω_c. This is because the Fano mirror has a large phase variation across the resonance, so the round-trip phase shifts of those modes are almost entirely determined by the phase change of the Fano mirror (the oscillation frequency keeps tracking the NC frequency). The FP modes do not exist in this region because the Fano mirror has a high reflectivity, dividing the WG into two independent "cavities". Therefore, the optical field would be restricted to either the left or right WG side, leading to two frequency-degenerate Fano modes but with different thresholds since $r_L \neq r_R$ (Fig. 2). The Fano mode with a higher threshold (lower Q-factor) is the RHS-Fano mode, whose field is concentrated in the NC and the RHS-WG. On the other hand, the mode with a lower threshold (higher Q-factor) is the LHS-Fano mode, whose field is concentrated in the NC and the LHS-WG.

Optics EXPRESS

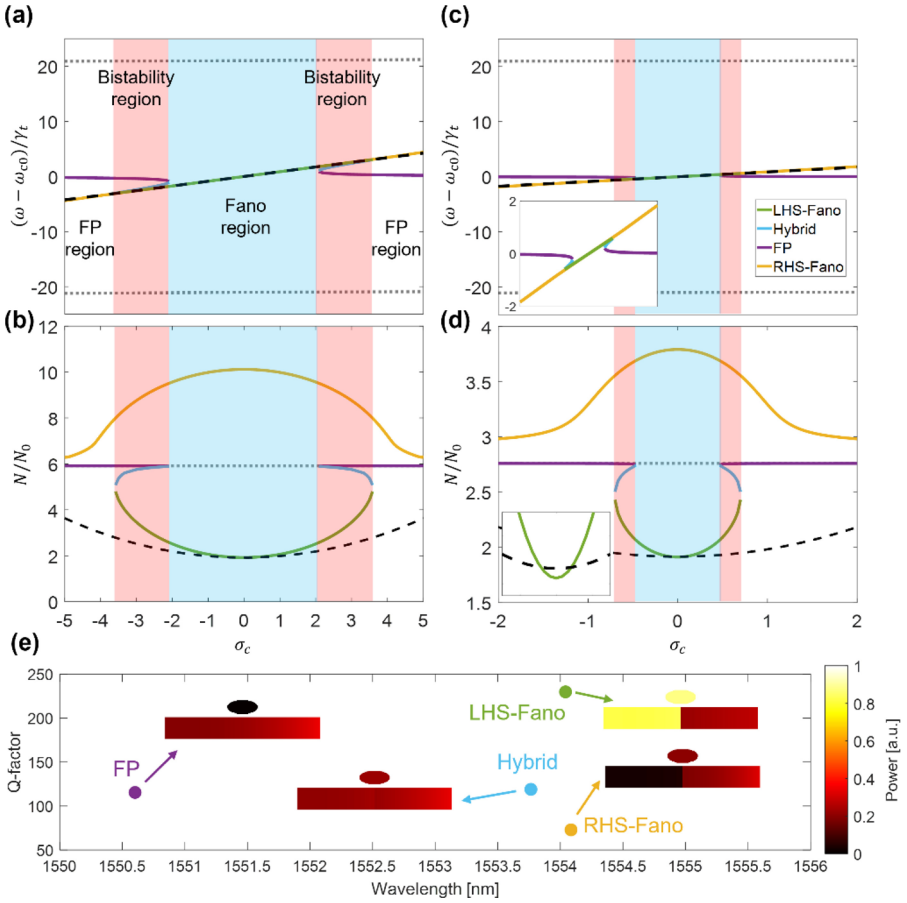

Fig. 2. (a), (c) Normalized oscillation frequency $(\omega - \omega_{c0})/\gamma_t$ and b), d) the corresponding laser threshold density N/N_0 of the modes versus the normalized NC frequency detuning $\sigma_c = (\omega_c - \omega_{c0})/\gamma_t$. (a), (b) are for $r_R = 0.3$, and (c), (d) are for $r_R = 0.7$. Here $\alpha = 0$. The colored lines represent four types of modes, including the LHS-Fano (green), hybrid (light blue), FP (violet), and RHS-Fano (orange) modes. The horizontal dotted lines represent the other longitudinal modes of the WG. The black dashed lines represent the Fano mode of the ordinary Fano laser as a reference with the same parameters but without feedback ($r_R = 0$). Three different regions are identified, including the FP (white), bistability (red-shaded), and Fano mode (blue-shaded) regions. The inset in (c) provides a detailed view of the modes within the normalized frequency range from -2 to 2, and the inset in (d) provides a detailed view of the region close to $\sigma_c = 0$. (e) The resonant wavelengths and Q-factors of the four different types of modes, extracted from (a) and (b) for an NC detuning of -3γ_t. The insets illustrate the spatial power distribution of each mode.

We first focus on the LHS-Fano mode. The LHS-Fano mode can be viewed as a mode where the field oscillates between the LHS mirror and a composite right mirror constituted by the original Fano mirror, the RHS-WG, and the RHS mirror. The reflection coefficient of such a composite mirror can be derived, again, by the transfer matrix approach as

$$r_{CMR}(\omega) = r_F(\omega) + \frac{r_R t_F^2(\omega)\exp[2ik(\omega,N)L_2]}{1 - r_R r_F(\omega)\exp[2ik(\omega,N)L_2]}. \tag{5}$$

Optics EXPRESS

Equation (5) shows that r_{CMR} is a combination of r_F and the reflection due to an external FP etalon. As seen, any variation in N impacts the external gain, subsequently influencing the feedback strength from the external FP. This, in turn, modifies both the amplitude and phase of the reflected field, resulting from the interplay between the fields reflected from the Fano mirror and the RHS mirror. Figure 1(b) shows the spectra of the reflectance and phase for the composite Fano mirror. The active composite mirror (yellow lines, assuming $N = 5N_0$) differs from the passive one (red lines) in the reflectance and phase when there is a detuning σ_c between mode frequency and NC frequency. Thus, in contrast to passive structures, adjusting σ_c modifies the system's loss and consequently N, causing shifts in both the amplitude and phase of r_{CMR}, even when $\alpha = 0$. Besides, the additional RHS-WG reflection and the high intrinsic dispersion of the FP etalon slightly increase the amplitude of r_{CMR} at ω_{c0} but largely narrow its bandwidth. As a result, the threshold of the LHS-Fano mode, although lower at ω_{c0} than the original Fano mode (without the external feedback) in the case of high reflection feedback, increases faster than the original Fano mode as the absolute detuning, $|\sigma_c|$, increases.

In the FP region, where ω_c is far detuned from ω_{c0}, the phase of r_{CMR} varies linearly with frequency, and the reflectance is low. In this situation, the LHS-Fano mode's phase-matching condition and gain-loss balance can no longer be simultaneously maintained. As a result, the FP mode, which is indifferent to changes in σ_c, overtakes and becomes the dominant lasing mode (see Supplement 1, Fig. S1). It is worth noting that the RHS-Fano mode can still exist in this region due to the much higher carrier density originating from the lower Q-factor ($r_R < r_L$), leading to a high reflectivity of the composite mirror. This composite mirror is the LHS composite mirror (reflecting light in the opposite direction compared to the RHS composite mirror), which has the same form as r_{CMR} in Eq. (5) but with L_2 and r_R replacing L_1 and r_L. This modification enlarges the phase variation range and makes it easier to fulfill the phase-matching condition. The threshold of the RHS-Fano mode is reduced in this region as more photons leak to the LHS-WG due to a reduction of the original Fano mirror reflectance. This elongates the photon lifetime and thus reduces the overall mirror loss.

Besides the Fano and the FP regions, there are two intermediate regions (bistability region) where four modes coexist. Because of a reduction of $|r_{CMR}|$, the threshold of the LHS-Fano mode increases rapidly with $|\sigma_c|$ and eventually vanishes at some point (creating a boundary between the FP and bistability region), cf. Figure 2 (red-shaded area). In the bistability region, there is an "intermediate" mode (hybrid mode) connecting the FP and LHS-Fano modes, whose spatial field distribution is located partially in the whole WG and partially in the NC (Fig. 2(e)). Such a hybrid mode has a larger detuning with respect to the NC frequency, so it has a larger threshold than the LHS-Fano mode. Notably, the RHS-Fano and the hybrid mode are unstable and cannot sustain lasing. (see the detailed discussions in Section 3.2 and Fig. 7). As seen from Fig. 2, the lasing FP mode extends across the FP and the bistability regions, reaching the boundaries of the Fano region on both the left and right sides. The lasing Fano mode extends across the Fano region and coexists with the FP mode within the bistability region.

Next, we investigate the dependence of the bistability on key laser parameters. Figure 2 illustrates the case of $\alpha = 0$. The threshold curves are symmetric for the case of zero detuning, $\sigma_c = 0$, due to the symmetric Lorentzian shape of the Fano mirror reflectance (Fig. 1(b)). When α is non-zero (e.g., $\alpha = 2$, a typical value for semiconductor InGaAsP quantum well lasers), an additional phase shift is introduced in the field due to the carrier-index coupling (see Eq. (3)). This results in a blueshift of the oscillation frequency ω at the lowest threshold point (Fig. 3), making the curves asymmetric. This effect also leads to multiple solutions, even in the ordinary Fano laser (see the black dashed line), with the upper solution being unstable. A finite α-parameter causes the phase-matching condition $\arg\{r_L\} + \arg\{r_F(\omega)\} + 2L_1 n\omega/c - \alpha\Gamma g_n(N - N_0)/2 = 2m\pi$ (where m is an integer) to interplay with the gain-loss balance condition. As a result, besides the primary solution, an alternative solution emerges distinct from ω_c. This secondary solution

Optics EXPRESS

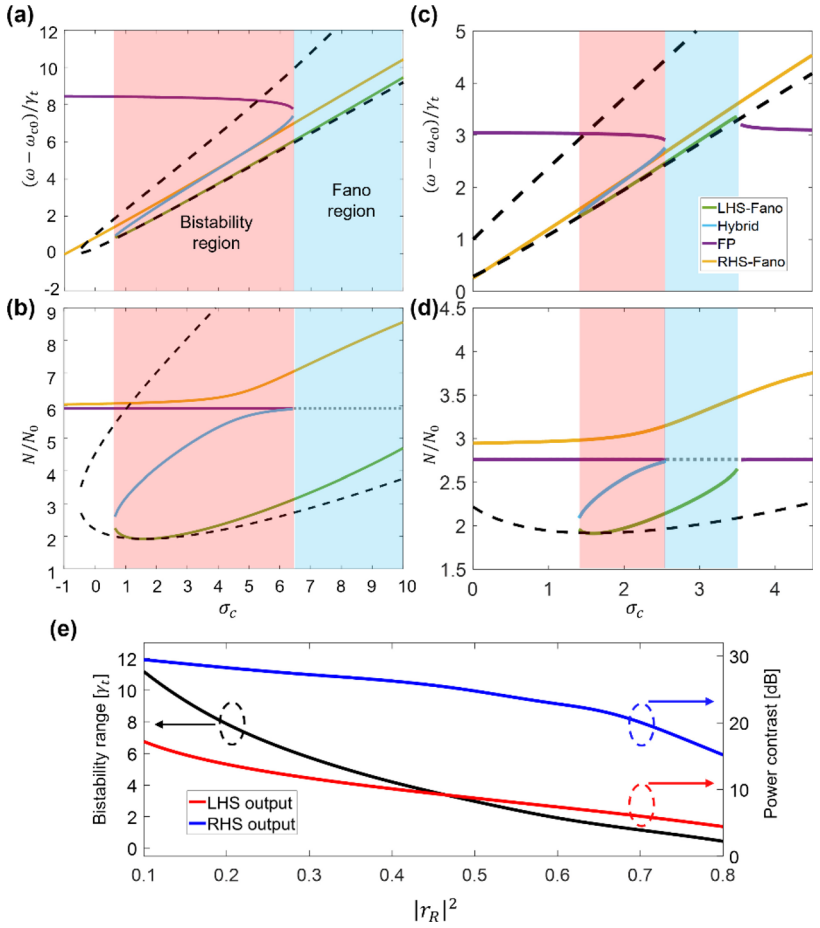

Fig. 3. (a), (c) Oscillation frequencies and (b), (d) the corresponding laser thresholds of the modes versus NC frequency detuning. (a) and (b) are for $r_R = 0.3$, and (c) and (d) are for $r_R = 0.7$. Here, $\alpha = 2$. The colored lines represent four types of modes, including the LHS-Fano (green), hybrid (light blue), FP (violet), and RHS-Fano (orange) modes. The black dashed lines represent the Fano mode of the ordinary Fano laser without feedback as a reference. Three different regions are highlighted with shaded backgrounds, consistent with Fig. 2, and the boundaries of these regions are determined the same way by the termination points of the LHS-Fano and FP modes' curves. (e) Bistability range (left axis) and power contrast between the mode with a higher output power and the mode with a lower output power (right axis) as a function of the RHS reflectance $|r_R|^2$. The power contrast is calculated for the NC detuning, where the LHS-Fano mode has the lowest threshold.

represents the hybrid mode in the feedback Fano laser framework. While, conventionally, this might be likened to a phase-locked state (typically denoting a stable synchronized state), in this scenario, it manifests as an unstable solution. As seen in Fig. 3, as σ_c increases (N will also increase), ω must shift more than the case of $\alpha = 0$ to enable a switch between the modes. Consequently, an increased α expands the bistability region.

The feedback intensity, represented by r_R, also plays an important role in the operation of the feedback Fano laser. As r_R increases ($r_R = 0.7$), cf. Figures 2(c), 2(d) and 3(c), 3d, the Fano and bistability regions shrink because the linewidth of the composite mirror, r_{CMR}, reduces (see Supplement 1, section 2). Figure 3(e) shows the bistability range and the associated output power

Optics EXPRESS

contrast as functions of r_R. The output power contrast is determined as the ratio of the mode with a higher optical output power (the LHS-Fano mode for the LHS output and the FP mode for the RHS output) to the mode with a lower output power (the FP mode for the LHS output and the LHS-Fano mode for the RHS output) at the lowest threshold point within the bistability region. In this case, we consider the power levels of the fields residing in the LHS (represented in red) and RHS-WG (represented in blue) regions. As mode switching can occur only when σ_c exceeds the bistability range (see section 4), the required energy for mode switching reduces for larger r_R. However, the power contrast decreases with r_R due to the escalating output power of the FP mode. A power contrast that is too low makes the device more susceptible to noise-induced bit-flip errors [31].

2.2. Role of feedback cavity length

Another critical parameter affecting the bistability is the effective external cavity length L_2, which depends on the WG's physical length and refractive index. For example, a variation of L_2 due to fabrication inaccuracies may alter the round-trip phase of the FP cavity and, thus, the bistability range. To examine the dependency on the WG length, we calculate the threshold and bistability range of the lowest threshold mode as a function of σ_c and L_2 (Fig. 4(a)). As seen, when the laser operates at the LHS-Fano mode, where $\sigma_c \approx 0$, the power in the RHS-WG is small, so the change of L_2 has a negligible effect on the lasing mode (see the middle area in Fig. 4(a)). Since the Fano laser frequency blueshifts along with the NC frequency blueshift [35], while it redshifts as L_2 increases (and vice versa) (see Supplement 1, Fig. S2a), the lasing condition of the Fano laser

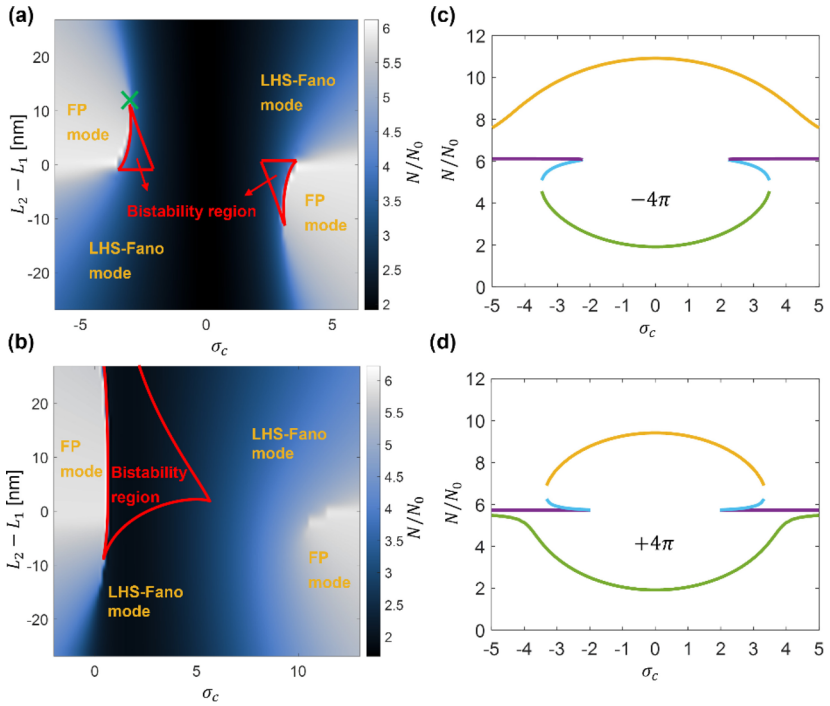

Fig. 4. The lowest threshold modes and the corresponding threshold carrier density as a function of RHS-WG length offset (L_2 -L_1) and NC detuning. L_1 is fixed at 5.3 μm. (a) is for $\alpha = 0$, and (b) is for $\alpha = 2$. Red closed curves mark the bistability regions. (c) and (d) are the threshold carrier density of the modes as a function of NC frequency detuning when L_2 is shorter (c) or longer (d) than L_1, with a WG phase shift of $\mp 4\pi$.

Optics EXPRESS

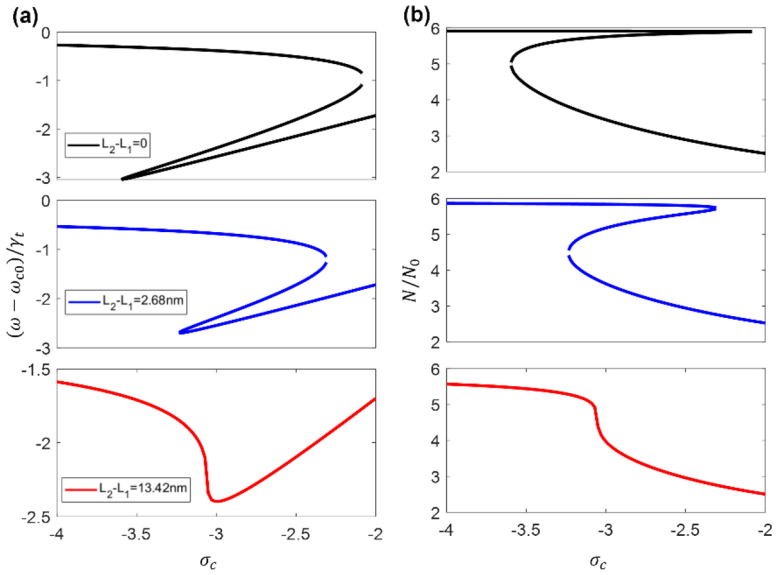

Fig. 5. The LHS-Fano mode variations versus NC frequency detuning for various RHS-WG length deviations. (a) shows the mode frequencies, and (b) shows the threshold carrier densities. The red curves represent the critical length at which the bistability region vanishes.

can still be met in the lower-left and upper-right areas in Fig. 4(a). Conversely, the oscillation condition cannot be met in the upper-left and lower-right regions, and the laser thus oscillates in the FP mode. The bistability regions appear between those two areas, with their areas decreasing as $|L_2 - L_1|$ increases. Here, L_1 is fixed at 5.3 µm. The selection of L_1 is based on achieving perfect phase matching between one of the longitudinal modes of the LHS-WG and the NC mode. This length is consistent with previous experiments where lasing was successfully demonstrated [15,16,47]. From the contour plots, one can examine the robustness of the bistability. We find that a stronger amplitude-phase coupling can significantly improve the robustness of the bistability region against (unintended) variations of L_2, as shown in Fig. 4(b). For example, the bistability range for a WG length, L_2, of around 5.3 µm is just 10 nm for $\alpha = 0$, which demands high fabrication accuracy. However, as α value increases to 2, the bistability region initially located on the blue side ($\sigma_c > 0$ when $\alpha = 0$) vanishes. In contrast, the region initially on the red side ($\sigma_c < 0$ when $\alpha = 0$) blueshifts and expands (as in Figs. 3(c) and 3(d)), indicating that the lasing state can be maintained even for a large deviation of L_2 up to 25 nm.

A notable observation for the larger variations of L_2 is the cyclical emergence of bistability. This occurs whenever the length of the RHS-WG aligns with 2π manifolds, as depicted in Fig. 4(c) and 4(d). Such behavior is anticipated in traditional passive structures, considering that completing an entire oscillation cycle of modulo 2π keeps the propagation phase consistent. However, it is noteworthy that excessively extending the WG can reduce the bistability region or even destroy it. Within an elongated external active WG, the optical field undergoes more pronounced amplification (assuming uniform pumping). As previously mentioned, this results in a decreased threshold carrier density for the FP mode, yielding a flatter composited mirror phase curve and consequently eliminating the bistability.

Figure 6 shows the LHS-Fano modes within one of the bistability regions when the RHS-WG length is slightly increased. As discussed in Section 2.1, the hybrid mode embodies characteristics of both LHS-Fano and FP modes. With an extension of the RHS-WG length, the bistability region can contract. Interestingly, there exists a specific length (see the red curve in Fig. 5, which

Optics EXPRESS

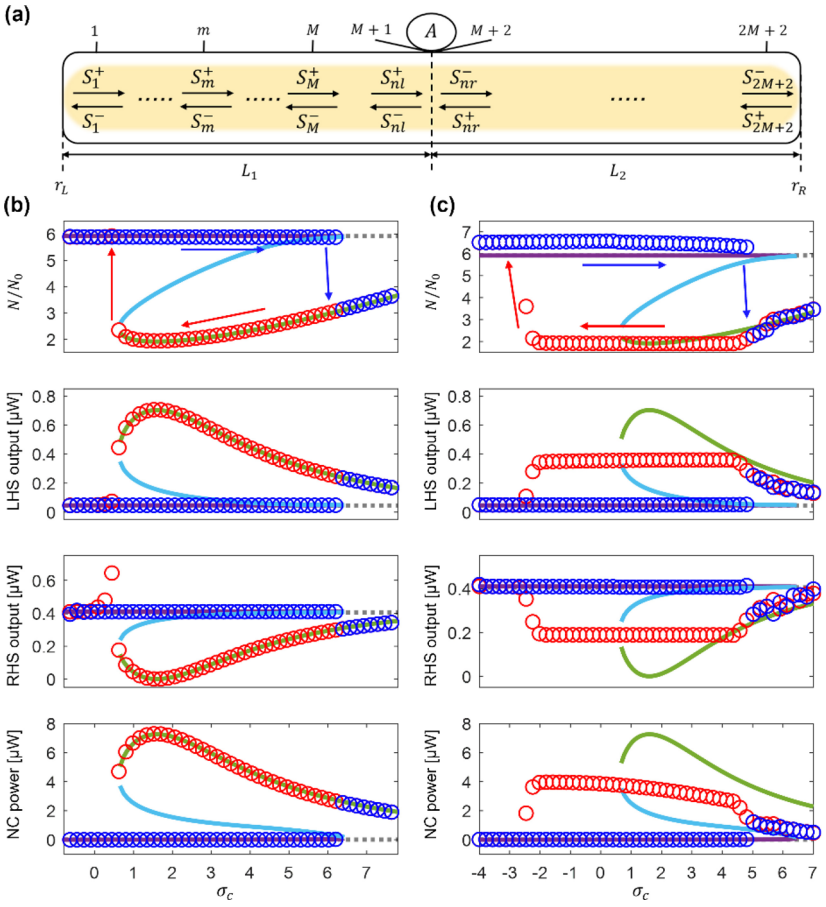

Fig. 6. (a) Schematics of the multisection model for the feedback Fano laser. (b), (c) Numerical solutions of the threshold carrier density (at the middle of LHS-WG), LHS/RHS output power, and the NC power using the multisection model. Here, $r_R = 0.3$, $\alpha = 2$. The colored circles represent the numerical solutions, including carrier diffusion (Eqs (6)–(9)), while the colored solid lines represent the semi-analytical solutions using Eq. (4). (b) is for an unrealistically large carrier diffusion rate of $D = D_{\max} = 11.5(\mathrm{m}^2/\mathrm{s})$, and (c) is with a diffusion rate of InGaAsP of $D = 6.027 \times 10^{-4}(\mathrm{m}^2/\mathrm{s})$ [39]. The red (blue) circles are the solutions when the NC frequency is scanned towards the lower (higher) frequency.

corresponds to the green cross in Fig. 4(a)) at which the hybrid mode merges with the FP and the LHS-Fano modes, bridging the two and creating, for a certain detuning, an infinite number of points satisfying the oscillation condition. As a result, the transition from the LHS-Fano mode to the FP mode occurs seamlessly without a mode jump, yet still accompanied by a substantial alteration in spatial power distribution. This phenomenon stems primarily from a phase "flattening" effect. Specifically, when assuming a constant N, even a minimal RHS-WG extension can significantly flatten the composite mirror phase curve on one of the spectral sides (see Supplement 1, Fig. S2a). Conversely, any increment in N can counterbalance this flattening of the phase curve (see Supplement 1, Fig. S2b). Collectively, these effects lead to multiple frequencies satisfying the phase condition. The abrupt power change without a mode jump may avoid transient relaxation oscillations and provide the potential to achieve rapid optical switching.

Optics EXPRESS

3. Dynamics of the bistable Fano laser

3.1. Steady state solution

The transfer matrix approach can be used to obtain the steady-state cavity modes but not the lasing dynamics. To simulate the dynamics of the laser, we use a multisection travelling wave model [16,36,37]. In this model, the WG is divided into 2 M sections. From the LHS mirror to the RHS mirror, the mth site is denoted as $m = 1,2...M+1, M+2,...2M+2$, as shown in Fig. 6(a), and we calculate the time evolution of the variables by the following plane wave propagation equations:

$$\begin{aligned}
S_m^+(t+\tau) &= \begin{cases} r_L S_1^-(t+\tau) & (m = 1, \text{LHS mirror}) \\ S_{m-1}^+(t)\exp[ik(\omega, N_{m-1}(t))v_g\tau] & (2 \le m \le M+1, \text{LHS - WG}) \end{cases} \\
S_m^-(t+\tau) &= S_{m+1}^-(t)\exp[ik(\omega, N_{m+1}(t))v_g\tau] \quad (1 \le m \le M) \\
S_m^+(t+\tau) &= \begin{cases} r_R S_{2M+2}^-(t+\tau) & (m = 2M+2, \text{RHS mirror}) \\ S_{m+1}^+(t)\exp[ik(\omega, N_{m+1}(t))v_g\tau] & (M+2 \le m \le 2M+1, \text{RHS - WG}) \end{cases} \\
S_m^-(t+\tau) &= S_{m-1}^-(t)\exp[ik(\omega, N_{m-1}(t))v_g\tau] \quad (M+3 \le m \le 2M+2)
\end{aligned} \tag{6}$$

The middle two sites, $M+1$ and $M+2$ are on the same spatial point but slightly left and right to the NC. Here, we alternatively denote $S_{M+1}^{\pm}$ and $S_{M+2}^{\pm}$ as $S_{nl}^{\pm}$ and $S_{nr}^{\pm}$, respectively. Combining with the coupled mode equation [32],

$$\frac{dA(t)}{dt} = -(i\delta(\omega) + \gamma_t)A(t) + i\sqrt{\gamma_c}S_{nl}^+(t) + i\sqrt{\gamma_c}S_{nr}^+(t), \tag{7}$$

$$S_{nl(nr)}^-(t) = -iS_{nr(nl)}^+(t) + \sqrt{\gamma_c}A(t), \tag{8}$$

and the carrier rate equation for each section [35]

$$\frac{dN_m(t)}{dt} = R_p - \frac{N_m(t)}{\tau_c} - \frac{\Gamma v_g g_n \sigma_0(|S_m^+(t)|^2 + |S_m^-(t)|^2)d}{V_d}(N_m(t) - N_0) + D\nabla^2 N_m(t). \tag{9}$$

Here, $S_m^{\pm}$ are the fields propagating towards (+) and away from (−) the NC at the mth section of the WG, $S_{nl(nr)}^{\pm}$ is the forward and backward propagating field on the left (nl) or right (nr) side (reference plane) of the NC in the WG, $A(t)$ is the NC field with $|A(t)|^2$ being the NC energy, $N_m(t)$ is the carrier density at the mth WG section, R_p is the pumping rate, τ_c is the carrier lifetime, v_g is the group velocity of the WG mode, $d = L_1/M$ is the length of each WG section, $\tau = d/v_g$ is the field propagation time within each WG section, $V_d = (d/(L_1 + L_2))V$ is the volume of the individual WG sections, with V being the total active region volume, σ_0 is a parameter relating the photon number in the cavity and the out-coupled power (see Supplement 1, section 3), and D is the carrier diffusion coefficient. The out-coupling through the LHS-WG (RHS-WG) end is $P_{L(R)} = |t_{L(R)}|^2|S_{1(2M+2)}^-|^2$.

Integrating the differential Eqs (7) and (9) with respect to time provides finite difference equations (see Supplement 1, section 3). The multisection model allows us to trace the time evolution and spatial distribution at every point within the device. We calculate the laser steady state for different NC frequencies by scanning from a negative to a positive value of σ_c and back. As a starting point, we choose uniform distributions of the field and carrier density within the WG. We determine the steady-state values after the transients, which are governed by relaxation oscillations above the threshold. After that, we change σ_c and set the initial values for the next detuning point as the steady-state solutions of the previous one. As seen in Figs. 6(b) and 6(c), when increasing the NC frequency (blueshift), the laser first stays on the FP mode and suddenly

Optics EXPRESS

jumps to the Fano mode as the Fano mirror reflectivity becomes high enough. Because of the lower threshold, the LHS-Fano mode will always dominate over the RHS-Fano mode. On the opposite side, when decreasing the NC frequency (redshift), the laser follows the LHS-Fano mode until it jumps to the FP mode, with the jumping point being different from the case where the nanocavity resonance is gradually blueshifted, leading to hysteresis and indicating the bistability. (Figure 6(b)).

When the carrier diffusion rate is sufficiently large, allowing carriers to spread throughout the active WG within their lifetime, i.e., $\sqrt{D\tau_c}>(L_1 + L_2)$, the carriers distribute nearly uniformly (see Supplement 1, Fig. S3, upper left). However, in the finite difference method, the diffusion rate cannot be larger than the length of section length d within a calculation timestep τ, more precisely $D \leq D_{\max} = d^2/(2\tau)$, otherwise, this would induce numerical instability [38]. For the section length d used in this simulation, $D_{\max} = 11.5(\mathrm{m}^2/\mathrm{s})$, which is much larger than the criteria $(L_1 + L_2)^2/\tau_c = 0.12$ $(\mathrm{m}^2/\mathrm{s})$ (refer to Supplement 1, Table S1). Using $D = D_{\max}$, the numerical solution of the steady-state solutions agrees with the semi-analytical solutions, which neglect the spatial variation of the carrier density. This result is expected and confirms the validity of our models.

In reality, however, the diffusion rate is much smaller than $D_{\max}$. As demonstrated in Fig. 6(c), using $D = 6.027\times10^{-4}(\mathrm{m}^2/\mathrm{s})$, which is an upper value for InGaAsP quantum wells [39], excited carriers tend to remain in their original location before recombining. Consequently, the carrier density in the RHS-WG remains higher than in the LHS-WG due to the weaker optical field for the LHS-Fano mode (see Supplement 1, Fig. S3, right column). This results in a lower stimulated recombination rate. Compared to the case of a large D, a smaller D leads to a stronger localization of carriers in the RHS-WG, providing increased gain. This gain increase compensates for the reduction in mirror loss, causing the reflectance of the composite Fano mirror to experience less variation when tuning σ_c. As a result, lasing in the LHS-Fano mode is sustained over a broader range of NC detuning, and is accompanied by less threshold/power variation across the bistability region, as shown in Fig. 6(c).

3.2. Dynamic behavior

Using the multisection model, we have numerically confirmed the stability of each mode in the feedback Fano laser (see Supplement 1, section 4). Figure 7 shows the time evolution of the NC energy, E_{NC}, and the carrier density, N, for four distinct modes located in the bistability region. The NC detuning σ_c is set as -3γ_t. As seen, the E_{NC} and N values for the RHS-Fano and hybrid modes, after large variations, eventually align with the level of the LHS-Fano mode. This transition into the LHS-Fano mode indicates their inherent instability. In contrast, the FP and LHS-Fano modes exhibit stability. Even after perturbations, they ultimately return to the states with N values matching the solution presented in Fig. 2(b). An interesting observation is the oscillatory behavior of the fields for the FP and LHS-Fano modes before they stabilize. This is attributed to the non-uniform carrier density distribution across the waveguide in the multisection model (which will be illustrated in Section 3), leading to a minor deviation from the steady-state solution of the oscillation condition. The stability of the FP and LHS-Fano modes defines the bistability region.

Next, we investigate the dynamic behavior of the laser when σ_c is modulated in time. Such a modulation scheme can be implemented electrically or optically, e.g., by carrier-induced refractive index change [40], leading to flip-flop action (Figs. 8(a) and 8(b)). Here, the pumping power is set at 40 times the threshold of the reference Fano laser, and the initial σ_c is chosen as $-3\gamma_t$, which is in the middle of the bistability region (see the red shaded area in Figs. 2(a), 2(b)). The carrier diffusion coefficient D is set to $D_{\max}$. At time $t = 0$, the laser is turned on and lases in the low threshold LHS-Fano mode. The Fano mode is characterized by having a small relaxation frequency and fast damping rate due to photon storage in the passive NC, which

Optics EXPRESS

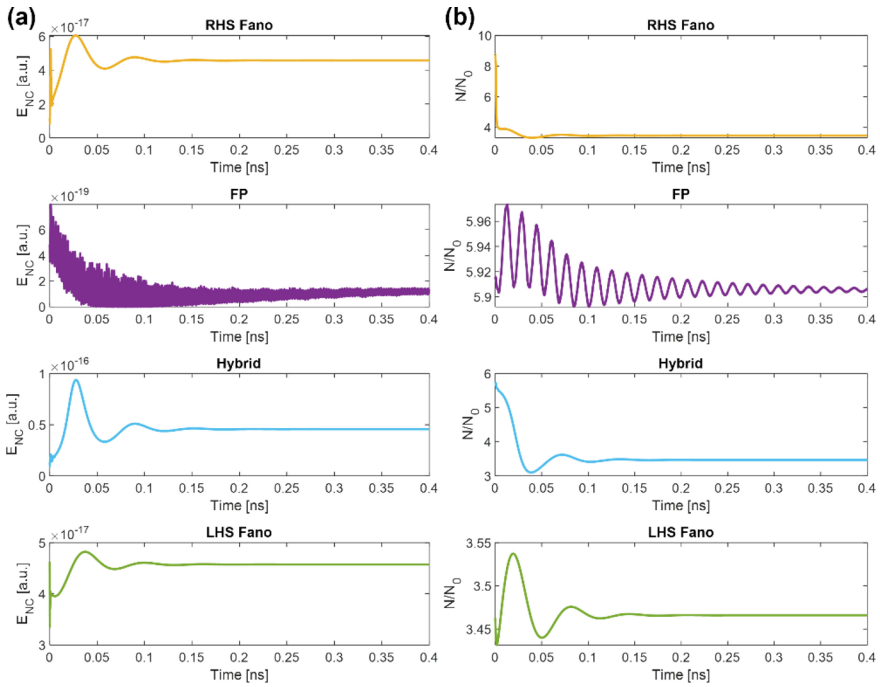

Fig. 7. Time evolution of the (a) NC energy, E_{NC}, and (b) carrier densities, N, for the RHS-Fano, FP, Hybrid, and LHS-Fano modes at an NC detuning $\sigma_c = -3\gamma_t$. The values of E_{NC} and N for both the RHS-Fano mode and the hybrid mode undergo large variations before eventually stabilizing at the same value as the LHS-Fano mode. The initial values of each mode are extracted from the steady-state oscillation condition (Eq. (4)).

reduces the interaction between the carrier and photon reservoirs [35]. A modulation pulse with a Gaussian shape is injected into the NC at 1.2 ns, causing a redshift of the NC frequency to $-5\gamma_t$ (this redshift can be realized even when only the blueshift is possible in reality, which will be explained in a later paragraph), making it cross the left boundary of the bistability region ($-3.6\gamma_t$), as shown in Figs. 2(a) and 2(b). The laser then transits from the LHS-Fano mode to the FP mode, characterized by a slower damping rate and faster relaxation oscillation. As seen, even after the detuning returns to its initial bias level, the laser remains in the FP mode. Following that, another pulse is injected at 2.4 ns, causing a blue shift of σ_c to $-1\gamma_t$, making it cross the bistability region's right boundary ($-2.1\gamma_t$). The laser thus switches back to the LHS-Fano mode. The simulation is also performed with a realistic diffusion rate of $D = 6.027 \times 10^{-4}$ (m^2/s) (the σ_c is initially set at γ_t and tuned from -4γ_t to 6γ_t accordingly), and the state switching is still observed (Fig. 8(b)). As demonstrated in Fig. 8(c), combining a finite α ($\alpha = 2$) and slower diffusion results in the entire bistability region having a very low carrier density for the LHS-Fano mode (e.g., $N \simeq 2$ for σ_c ranging from -2γ_t to 5γ_t). A larger extinction ratio can be attained during the mode-switching compared to the scenario with zero α and rapid diffusion (Fig. 8(a)). The lower parts of Figs. 8(a) and 8(b) show the output power from the LHS mirror (the second row, red lines), which has the opposite time evolution as the output power from the RHS mirror (the third row, blue lines). This is because the LHS-WG field is much stronger for the Fano mode than the FP mode, while the RHS-WG field is much less (see Supplement 1, Fig. S3). Such an intrinsic anti-correlation between the power levels from the different ports distinguishes our feedback Fano laser from ordinary flip-flop devices. This feature makes it possible to construct a

Optics EXPRESS

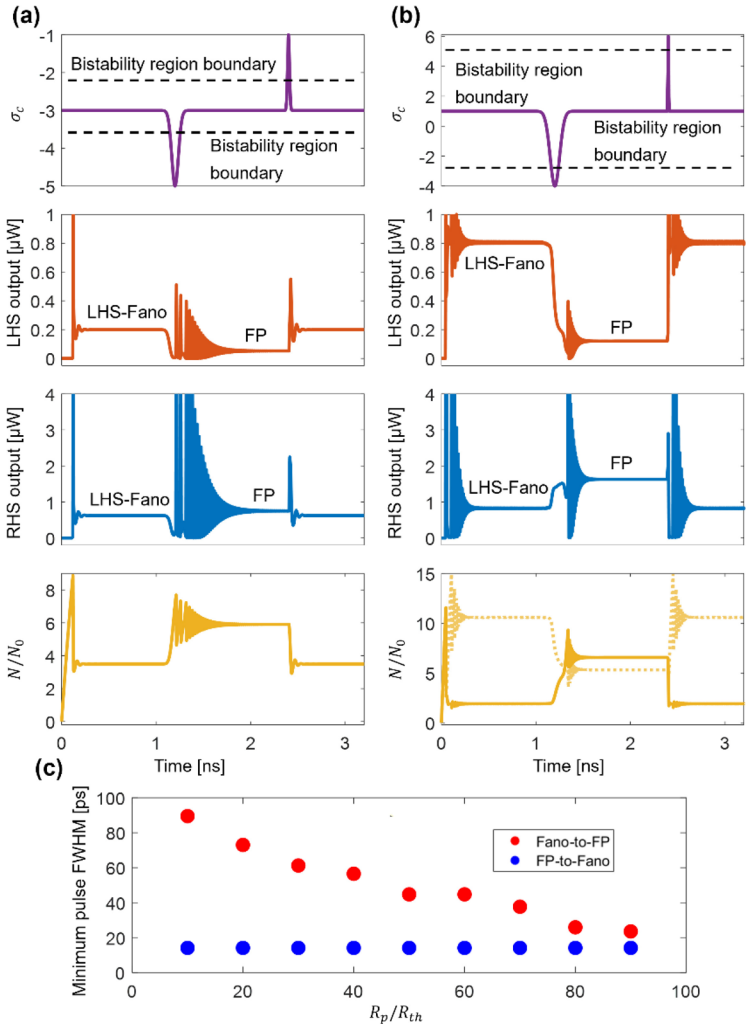

Fig. 8. Flip-flop action using the feedback Fano laser. Here $r_R = 0.3$. (a) The NC resonance frequency detuning, initially set at -3γ_t, redshifts to -5γ_t, and then blueshifts to -γ_t at $t = 1.2$ ns and $t = 2.4$ ns, respectively (violet line). Shown below are the LHS output power (red line), RHS output power (blue line), and carrier density (yellow line, at the midpoint of the LHS-WG). Here $\alpha = 0$ and $D = D_{\max}$. (b) The NC resonance frequency detuning, initially set at γ_t, redshifts to -4γ_t and then blueshifts to 6γ_t. Below are the LHS output power, RHS output power, and carrier density (yellow solid line, at the midpoint of the LHS-WG; yellow dashed line, at the midpoint of the RHS-WG). Here, $\alpha = 2$ and $D = 6.027 \times 10^{-4}(\mathrm{m}^2/\mathrm{s})$. (c) Minimum pulse width (FWHM) required to trigger the mode switching as a function of laser pumping rate R_p, which has been normalized to the laser threshold R_{th}. Red dots represent the Fano-to-FP mode switching, and blue dots represent the FP-to-Fano mode switching.

shift register by interconnecting the anti-correlation port to the subsequent flip-flop in a series arrangement [41].

As expected, the modulating pulse must surpass a specific threshold to enable the mode switching, imposing requirements on both the temporal width and amplitude of the modulating pulse. The laser state will remain unaltered if the modulating pulse peak power falls below these threshold values. Conversely, when the pulse exceeds the threshold, the laser requires a certain

Optics EXPRESS

duration to alter and stabilize the carrier density level. From the simulations of the switching dynamics (Fig. 8(a)), one can extract the shortest pulse width (full width at half maximum, FWHM) capable of triggering the mode switching (Fig. 8(c)). As seen, the minimum FWHM of the pulse for the Fano-to-FP switching depends on the pump power and is longer than for the FP-to-Fano switching. This is because the threshold carrier density of the FP mode is much larger than the Fano mode due to the much lower Q-factor (see the fourth row of Fig. 8(a)). This implies that the Fano-to-FP process mimics the laser turn-on process, which needs time to accumulate carrier population and therefore has a delay [31]. Indeed, Fig. 8(c) shows that the minimum FWHM of the triggering pulse for the Fano-to-FP process has the opposite relation with the pumping power qualitatively aligned with the variation of laser delay time. On the other hand, the FP-to-Fano switching leads to a lowering of the average carrier density. This process relies on stimulated emission, which decreases the carrier population much faster than raising it. The process here is like a laser Q-switching [42]. To completely change the laser state, one needs to wait for the pulse to be fully released, whose trailing edge largely depends on the photon lifetime, which relates to the mirror loss and cavity length rather than the pumping rate [42]. The minimum FWHM of the triggering pulse in the FP-to-Fano switching is, therefore, shorter than Fano-to-FP switching and is insensitive to the pumping rate.

Besides the pump power, the NC detuning also affects the minimum FWHM of the triggering pulse. Figure 9(a) depicts the extracted minimum pulse width as a function of σ_c. Here, σ_c is initially set at -3γ_t with the same parameters used in Fig. 9(a). The NC detuning will be later tuned to a certain value. The range it tunes is defined as the modulation depth. As seen, the FWHM of the triggering pulse is inversely related to the detuning of the nanocavity. Once the bistability boundary is surpassed, the minimum FWHM decreases with the change of σ_c for both the Fano-to-FP and FP-to-Fano cases. Decreasing the minimum pulse width would reach a lower limit, corresponding to the Fano mirror being either fully transparent (transitioning from Fano-to-FP mode, red curve) or entirely blocked (transitioning from FP-to-Fano mode, blue curve). In the former case, the carrier population's buildup would not be hindered by the stimulation emission from the field trap inside the Fano cavity. In the latter case, the Fano mirror can half the FP cavity length and decrease the photon lifetime. In both situations, the laser operates as either a "pure" FP laser or a Fano laser, and the mode buildup time can be shorter than a laser with a partially transparent mirror. As seen in Fig. 9(a), the lower limit of both the Fano-to-FP and FP-to-Fano process is below 50ps, considerably faster than the previous photonic crystal optical flip-flop devices [7], which require several nanoseconds to deplete a large number of trapped carriers.

We now estimate the energy requirement for the triggering pulse used to shift the NC frequency. We assume that the NC is illuminated by an external source, which modulates the NC resonant frequency due to the index change caused by the free carriers [43] generated through two-photon absorption. Although the free carrier effect would typically only result in a blueshift of the resonance [43], one can design the NC to have an initial red detuning σ_i outside the bistability region and then apply a bias to bring the laser back into the bistability region. For example, in Fig. 8(a), we have a cold cavity detuning σ_i = -5γ_t and then apply a constant NC shift of 2γ_t so that the initial detuning is biased at σ_b = -3γ_t. By subsequently applying a triggering pulse or turning off the bias, it is possible to traverse both sides of the bistability region, thereby realizing mode switching. The bias power P_b can be estimated using the relation [40] $|\sigma_b - \sigma_i|\gamma_t = K_c N_c$ and $G_{TPA}(P_b/\gamma_{cp})^2 = N_c/\tau_c$, where K_c is the nonlinear coefficient due to free carrier induced dispersion, N_c is the carrier density inside the NC and γ_{cp} is the coupling rate of the NC for the external modulation light source, leading to a coupling Q-factor of $Q_{cp} = \omega_{c0}/(2\gamma_{cp})$. The paramater $G_{TPA} = \beta_{TPA}c^2/(2\hbar\omega_{c0}n^2V_{FCA}^2)$ is the two-photon generation coefficient [40], where β_{TPA} is the two-photon absorption coefficient, and V_{FCA} is the nonlinear mode volume due to free carrier absorption. Here, we have assumed that the switching speed is much slower than the

Optics EXPRESS

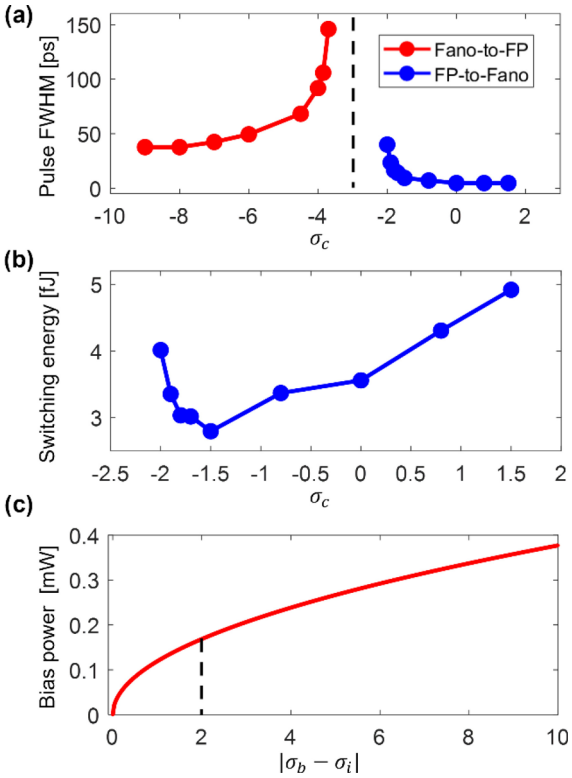

Fig. 9. (a) Triggering pulse width as a function of the NC detuning, with a pumping rate $R_p = 40R_{th}$. Red lines represent Fano-to-FP switching, and blue lines represent FP-to-Fano switching. The initial detuning is $\sigma_i = -5\gamma_t$, and then biased to $\sigma_b = -3\gamma_t$. The black dashed line marks the NC detuning after applying the bias. (b) Corresponding triggering pulse energy for the FP-to-Fano switching in (a), assuming an H1-type nanocavity with detuning induced by the free carrier effects. (c) Bias power as a function of $|\sigma_b - \sigma_i|$, with the black dashed line indicating the bias setting used in (a) and (b).

carrier relaxation rate, which is a good approximation for an NC with an ultrasmall mode volume, as the ultrasmall mode volume would accelerate the carrier diffusion [40,44,45]. In addition, we neglect the optical nonlinearities induced bistability caused by the lasing mode in the NC itself [46] and consider that a higher-order mode of the NC other than the Fano mode is excited. This approach enables efficient modulation of the NC without disturbing the original Fano laser system, as the higher-order mode exhibits weak coupling to the WG, so the NC can maintain a much large Q_{cp} [47]. We can then calculate the bias power $P_b = \sqrt{|\sigma_b - \sigma_i|\gamma_t\gamma_{cp}^2/K_c G_{TPA}\tau_c}$ and the energy cost for the triggering pulse $E_p \approx \sqrt{\Delta T\gamma_t\gamma_{cp}^2/K_c G_{TPA}}\left(\sqrt{|\sigma_c - \sigma_i|} - \sqrt{|\sigma_b - \sigma_i|}\right)$ [48]. Here, ΔT is the pulse width. In the simulations, we chose a Q_{cp} of 10^4 and a V_{FCA} of 0.108 μm^3, which are reasonable values for an H1-type photonic crystal NC [49].

Figure 9(b) shows the energy cost of the triggering pulse (FP-to-Fano) for an initial NC detuning $\sigma_i = -5\gamma_t$ and an after-bias detuning $\sigma_b = -3\gamma_t$. As seen, a trade-off exists between the switching pulse width and the absolute detuning σ_c caused by the pulse. The bias power is on the order of milliwatts (Fig. 9(c)), e.g., 0.18 mW for $|\sigma_b - \sigma_i| = 2$, and increases monotonically with $|\sigma_b - \sigma_i|$. The optimal (lowest) energy occurs approximately $0.5\gamma_t$ ($\sigma_c = -1.5\gamma_t$) away from the boundary of the bistability region. The lowest switching energy reaches 2.8 fJ/bit for the

Optics EXPRESS

FP-to-Fano process. The energy consumption can be further reduced by increasing the Q-factor or decreasing the mode volume of the NC, as a larger Q/V enhances the field strength and, thus, the optical nonlinearities in the NC [40]. For example, if Q_{cp} were to increase tenfold, the pulse energy could be reduced to ~0.28 fJ/bit, and the bias power could be decreased to ~16 μW. One should note that extra power is needed for pumping the laser. However, such pumping power can be significantly reduced (sub μW) by using nanolasers [26].

Compared to the dual-coupled NC system [29], which can also generate fast flip-flops with low energy consumption, our NC-WG coupled system uses a different mechanism. In the NC-WG system, the two states – the Fano and the FP mode – maintain stability within the optical bistability region (see Supplement 1, section 4). This optical bistability can be interpreted as either a pairing of two saddle-node bifurcations or a subcritical pitchfork bifurcation with high-order nonlinearities. As a result, when activated, the states exhibit a pronounced contrast and enhanced resilience to external disturbances. Moreover, the specific state it adopts is directly influenced by the initial conditions. This starkly contrasts the states formed by the supercritical pitchfork bifurcation in the dual-coupled NC system [29]. Here, the activated state is randomly chosen as the system is initiated. Furthermore, the supercritical pitchfork bifurcation in [29] could also lead to the Hopf bifurcation, resulting in unstable states characterized by rapid oscillations. Such a limitation may potentially restrict the operational parameters for flip-flops.

4. Conclusion

In conclusion, we propose a Fano laser with strong optical feedback that implements optical bistability between a Fano and a Fabry-Perot mode. We analyze the lasing modes of the system using a semi-analytical approach, which agrees well with the numerical approach based on a multisection traveling wave method. Our results show that strong field localization in the nanocavity of the Fano laser, paired with the strong dispersion of the Fano mirror, enables efficient control of the Q-factor and, consequently, the laser threshold. This feature allows for switching the lasing state by controlling the mirror loss, which can be achieved by a local modulation only in the nanocavity instead of the entire laser system. This is in contrast to conventional bistable devices, which rely on changes in the susceptibility of a nonlinear medium to facilitate state-switching.

We analyze the impact of crucial laser parameters on the bistability characteristics of the feedback Fano laser, including the nanocavity resonance detuning, the linewidth enhancement factor, the feedback strength, and the length of the external cavity. Our results suggest that an energy-efficient flip-flop device can be realized using a quantum dot laser, characterized by its near-zero α, combined with a high feedback strength, leading to a small bistability region and low energy consumption. On the other hand, for devices prioritizing stability and noise resistance, a quantum well laser, characterized by a finite α and moderate reflection feedback, will provide a wider bistability domain, ensuring greater resilience against external noise and fluctuations. Furthermore, when considering a realistic carrier diffusion rate, the laser enlarges its bistability region and output contrast compared to infinitely high diffusion rate scenarios.

As an application, we investigate the temporal dynamics of the feedback Fano laser for flip-flop action, taking into account the effects of spatial carrier diffusion. The feedback Fano laser exhibits fast switching, with characteristic times depending on the turn-on delay and stimulated emission of the laser, which can be tuned by the pump power. The switching energy can be optimized depending on the Q/V of the nanocavity. When integrated within a microscopic structure, our proposed design reveals the exciting possibility of sub-fJ/bit operations for integrated on-chip computing.

Funding. Danmarks Grundforskningsfond (DNRF147); Villum Fonden (42026, EXTREME); H2020 European Research Council (834410 Fano).

Acknowledgements. We thank G. Dong for his inspiration and insightful discussions.

Optics EXPRESS

Disclosures. The authors declare no competing interests.

Data availability. Data underlying the results presented in this paper may be obtained from the authors upon reasonable request.

Supplemental document. See Supplement 1 for supporting content.

References

1. M. M. Mano and C. R. Kime, "*Logic and Computer Design Fundamentals, Global Edition*," (Pearson Education Limited, 2015).
2. J. M. Liu and Y. C. Chen, "Optical flip-flop," Electron. Lett. **21**(6), 236 (1985).
3. R. S. Tucker and K. Hinton, "Energy consumption and energy density in optical and electronic signal processing," IEEE Photonics J. **3**(5), 821–833 (2011).
4. H. J. S. Dorren, D. Lenstra, Y. Liu, *et al.*, "Nonlinear polarization rotation in semiconductor optical amplifiers: theory and application to all-optical flip-flop memories," IEEE J. Quantum Electron. **39**(1), 141–148 (2003).
5. Y. Naito, S. Shimizu, T. Kato, *et al.*, "Investigation of all-optical latching operation of a monolithically integrated SOA-MZI with a feedback loop," Opt. Express **20**(26), B339 (2012).
6. A. Trita, G. Mezõsi, M. Zanola, *et al.*, "Monolithic All-Optical Set-Reset Flip-Flop operating at 10 Gb/s," IEEE Photon. Technol. Lett. **25**(24), 2408–2411 (2013).
7. K. Nozaki, A. Shinya, S. Matsuo, *et al.*, "Ultralow-power all-optical RAM based on nanocavities," Nat. Photonics **6**(4), 248–252 (2012).
8. D. Fitsios, K. Vyrsokinos, A. Miliou, *et al.*, "Memory Speed Analysis of Optical RAM and Optical Flip-Flop Circuits Based on Coupled SOA-MZI Gates," IEEE J. Select. Topics Quantum Electron. **18**(2), 1006–1015 (2012).
9. L. Liu, R. Kumar, K. Huybrechts, *et al.*, "An ultra-small, low-power, all-optical flip-flop memory on a silicon chip," Nat. Photonics **4**(3), 182–187 (2010).
10. M. T. Hill, H. J. S. Dorren, T. de Vries, *et al.*, "A fast low-power optical memory based on coupled micro-ring lasers," Nature **432**(7014), 206–209 (2004).
11. C.-H. Chen, S. Matsuo, K. Nozaki, *et al.*, "All-optical memory based on injection-locking bistability in photonic crystal lasers," Opt. Express **19**(4), 3387 (2011).
12. A. E. Miroshnichenko, S. Flach, and Y. S. Kivshar, "Fano resonances in nanoscale structures," Rev. Mod. Phys. **82**(3), 2257–2298 (2010).
13. M. F. Limonov, M. V. Rybin, A. N. Poddubny, *et al.*, "Fano resonances in photonics," Nat. Photonics **11**(9), 543–554 (2017).
14. J. Mørk, Y. Chen, and M. Heuck, "Photonic crystal Fano laser: terahertz modulation and ultrashort pulse generation," Phys. Rev. Lett. **113**(16), 163901 (2014).
15. J. Mørk, Y. Yu, T. S. Rasmussen, *et al.*, "Semiconductor Fano lasers," IEEE J. Select. Topics Quantum Electron. **25**(6), 1–14 (2019).
16. Y. Yu, W. Xue, E. Semenova, *et al.*, "Demonstration of a self-pulsing photonic crystal Fano laser," Nat. Photonics **11**(2), 81–84 (2017).
17. Y. Yu, A. Sakanas, A. R. Zali, *et al.*, "Ultra-coherent Fano laser based on a bound state in the continuum," Nat. Photonics **15**(10), 758–764 (2021).
18. T. S. Rasmussen, Y. Yu, and J. Mørk, "Suppression of Coherence Collapse in Semiconductor Fano Lasers," Phys. Rev. Lett. **123**(23), 233904 (2019).
19. D. Bekele, Y. Yu, K. Yvind, *et al.*, "In-Plane Photonic Crystal Devices using Fano Resonances," Laser Photonics Rev. **13**(12), 1900054 (2019).
20. O. Painter, R. K. Lee, A. Scherer, *et al.*, "Two-Dimensional Photonic Band-Gap Defect Mode Laser," Science **284**(5421), 1819–1821 (1999).
21. Y. Gong and J. Vuckovic, "Photonic crystal cavities in silicon dioxide," Appl. Phys. Lett. **96**(3), 031107 (2010).
22. K.-Y. Jeong, Y.-S. No, Y. Hwang, *et al.*, "Electrically driven nanobeam laser," Nat. Commun. **4**(1), 2822 (2013).
23. G. Dong, M. Xiong, E. Dimopoulos, *et al.*, "Fano Laser Based on a Photonic Crystal Nanobeam Cavity," in *CLEO, San Jose, United States* (2022).
24. K. Saito and R. Ito, "Buried-heterostructure AlGaAs lasers," IEEE J. Quantum Electron. **16**(2), 205–215 (1980).
25. S. Matsuo, A. Shinya, T. Kakitsuka, *et al.*, "High-speed ultracompact buried heterostructure photonic-crystal laser with 13 fJ of energy consumed per bit transmitted," Nat. Photonics **4**(9), 648–654 (2010).
26. E. Dimopoulos, A. Sakanas, A. Marchevsky, *et al.*, "Electrically-Driven Photonic Crystal Lasers with Ultra-low Threshold," Laser Photon. Rev. **16**(11), 2200109 (2022).
27. E. Dimopoulos, M. Xiong, A. Sakanas, *et al.*, "Experimental demonstration of a nanolaser with a sub-μA threshold current," Optica **10**(8), 973 (2023).
28. N. Ismail, C. C. Kores, D. Geskus, *et al.*, "Fabry-Pérot resonator: spectral line shapes, generic and related Airy distributions, linewidths, finesses, and performance at low or frequency-dependent reflectivity," Opt. Express **24**(15), 16366 (2016).
29. P. Hamel, S. Haddadi, F. Raineri, *et al.*, "Spontaneous mirror-symmetry breaking in coupled photonic-crystal nanolasers," Nat. Photonics **9**(5), 311–315 (2015).
30. Y. Yu, A. R. Zali, and J. Mørk, "Theory of linewidth narrowing in Fano lasers," Phys. Rev. Res. **4**(4), 043194 (2022).

Optics EXPRESS

31. L. A. Coldren and S. Corzine, "*Diode Lasers and Photonic Integrated Circuits*," (Wiley, 1995).
32. S. Fan, W. Suh, and J. D. Joannopoulos, "Temporal coupled-mode theory for the Fano resonance in optical resonators," J. Opt. Soc. Am. A **20**(3), 569 (2003).
33. C. Henry, "Theory of the linewidth of semiconductor lasers," IEEE J. Quantum Electron. **18**(2), 259–264 (1982).
34. M. Saldutti, T. S. Rasmussen, M. Gioannini, *et al.*, "Modal Properties of Photonic Crystal Cavities and Applications to Lasers,," Opt. Lett. **45**(21), 6022 (2020).
35. T. S. Rasmussen, "Light-matter interaction and laser dynamics in nanophotonic structures," Technical University of Denmark, (2020).
36. A. J. Lowery, "New dynamic semiconductor laser model based on the transmission-line modelling method," IEEE Proceedings J (Optoelectronics) 134 (1987).
37. B. Tromborg, H. Olesen, X. Pan, *et al.*, "Transmission line description of optical feedback and injection locking for fabry-perot and dfb lasers," IEEE J. Quantum Electron. **23**(11), 1875–1889 (1987).
38. H. P. Langtangen and S. Linge, "*Finite Difference Computing with PDEs: A Modern Software Approach*," (Springer, 2017).
39. M. Levinshtein, S. Rumyantsev, and M. Shur, "*Handbook Series on Semiconductor Parameters*," (World Scientific, 1996).
40. Y. Yu, E. Palushani, M. Heuck, *et al.*, "Switching characteristics of an InP photonic crystal nanocavity: Experiment and theory," Opt. Express **21**(25), 31047 (2013).
41. B. Holdsworth and C. Woods, "*Digital Logic Design*," 4th ed., (Oxford, 2002).
42. U. Keller, "Q-Switching," in *Ultrafast Lasers*, (Springer, 2021), Chap. 8.
43. B. R. Bennett, R. A. Soref, and J. A. D. Alamo, "Carrier-induced change in refractive index of InP, GaAs and InGaAsP," IEEE J. Quantum Electron. **26**(1), 113–122 (1990).
44. M. Saldutti, Y. Yu, P. T. Kristensen, *et al.*, "Carrier dynamics in nonlinear photonic nanocavities with extreme dielectric confinement," in *2022 IEEE Photonics Conference (IPC)* (2022), pp. 1–2.
45. M. Saldutti, Y. Yu, G. Kountouris, *et al.*, "Carrier diffusion in semiconductor nanoscale resonators," arXiv, arXiv:2308.16715 (2023).
46. Y. Yu, Y. Chen, H. Hu, *et al.*, "Nonreciprocal transmission in a nonlinear photonic-crystal Fano structure with broken symmetry," Laser & Photon. Rev. **9**(2), 241–247 (2015).
47. G. Dong, S. L. Liang, A. Sakanas, *et al.*, "Cavity dumping using a microscopic Fano laser," Optica **10**(2), 248 (2023).
48. T. S. Rasmussen, Y. Yu, and J. Mørk, "All-optical nonlinear activation function for neuromorphic photonic computing using semiconductor Fano lasers," Opt. Lett. **45**(14), 3844 (2020).
49. M. Saldutti, M. Xiong, E. Dimopoulos, *et al.*, "Modal Properties of Photonic Crystal Cavities and Applications to Lasers," Nanomaterials **11**(11), 3030 (2021).